A novel titanium alloy for load-bearing biomedical implants: Evaluating the antibacterial and biocompatibility of Ti536 produced via electron beam powder bed fusion additive

A Novel Titanium Alloy for Load-Bearing Biomedical Implants: Evaluating the Antibacterial and Biocompatibility of Ti536 Produced through EB-PBF

Amir behjat[a,b], Saber Sanaei[a], Mohammad Hossein Mosallanejad [b], Masoud Atapour[a]*, Mohammadali Sheikholeslam[c], Luca Iuliano[b], Abdollah Saboori[b]*

[a] *Department of Materials Engineering, Isfahan University of Technology, Isfahan 84156-83111, Iran*
[b] *Integrated Additive Manufacturing Center, Department of Management and Production Engineering, Politecnico di Torino, Corso Duca degli Abruzzi 24,10129 Torino, Italy*
[c] *Department of Biomaterials, Tissue Engineering and Nanotechnology, School of Advanced Technologies in Medicine, Isfahan University of Medical Sciences, Isfahan 81746-73461, Iran*

**Corresponding author: Abdollah.saboori@polito.it, +39-0110907285*
**Co-corresponding author: M.atapour@cc.iut.ac.ir, +98-03133915735*

Abstract

Additive manufacturing (AM) of Ti-based biomedical implants is a pivotal research topic due to the AM great advantage in producing implants with complicated geometries. Although Ti alloys are featured with desirable mechanical properties and biocompatibility, one major drawback is the alloy's lack of inherent antibacterial properties, which increases the risk of postoperative infections. Hence, the current research systematically investigates the bio-corrosion, antibacterial properties, and cell biocompatibility of the novel Ti6Al4V-7Cu alloy (Ti536), a potential candidate composition for biomedical applications recently developed by Electron Beam Powder Bed Fusion (EB-PBF). The microstructural characterization revealed grain refinement and the formation of Ti_2Cu precipitates with different morphologies and sizes in the Ti matrix. Electrochemical tests showed that Cu content minimally influenced the corrosion current density, while it slightly affected the stability, defect density, and chemical composition of the passive film. According to the findings, the Ti536 alloy demonstrated enhanced antibacterial properties without compromising its cell biocompatibility and corrosion behavior, thanks to the presence of Ti_2Cu precipitates. This can be attributed to both the release of Cu ions and the Ti_2Cu precipitates. The current study suggests that the EB-PBF fabricated Ti536 sample is an ideal material for load-bearing applications in the medical sector. This research also offers an alloy design roadmap for novel biomedical Ti-based alloys with superior biological performance using additive manufacturing methods.

Keywords: Electron beam powder bed fusion; Additive manufacturing; In-situ alloying; corrosion; antibacterial property; MTT assay.

1. Introduction

Additive Manufacturing (AM) has revolutionized the production of patient-specific implants, allowing for the creation of customized implants to meet the unique requirements of individual patients. AM-based techniques enable the fabrication of complex-shaped implants with multifunctional and interconnected porous architectures that are difficult to produce using traditional methods [1,2]. These properties have contributed to the rapid expansion of AM methods in the fields of dental, craniofacial, spinal cord, and skeletal bone regeneration [3,4]. Powder bed fusion (PBF), among the most widely utilized AM methods for producing implants, is based on the selective melting of metal powder layer by layer using electron or laser beams [5]. Electron beam powder bed fusion (EB-PBF), also referred to as electron beam melting (EBM), utilizes high-energy electron beams to melt metal powder particles. Unlike laser-based powder bed fusion (LPBF), which is performed under an inert gas environment, EB-PBF necessitates a high vacuum to prevent smoking, contamination, and powder oxidation. The vacuum condition also enhances energy efficiency, particularly for reactive metals like titanium [6].

Although medical devices significantly enhance the life quality of the patients, device-associated infections or inflammations remain a primary concern despite stringent antiseptic operating protocols [7,8]. According to reports, inflammation was observed in 90% of all implants, with 50% of all implants exhibiting signs of irreversible tissue damage [8]. Furthermore, these implants often fail to integrate well with the host tissue, resulting in severe complications such as implant rejection and failure, ultimately necessitating the need for arduous revision surgeries. As a result, the prevalence of implant-associated infections has significantly impeded the widespread adoption of medical alloys within the medical industry [9]. Microbial biofilms are considered the major causative agent of implant-associated infections. The formation of these biofilms can result in implant loosening and interfere with the deposition of new bone. In order to mitigate the risk of infection in clinical settings, it is imperative that biomedical materials exhibit antibacterial properties [10]. For the case of titanium alloys, surface modification has been employed so far to impart antibacterial functionality, generally by integrating an antibacterial element into its surface coating [11,12]. Despite their advantages, antibacterial coatings have limited efficacy in the long term, as they tend to detach from the implant during clinical use and release excessive metallic ions into the human body [9]. As a result, significant efforts have been directed toward creating innovative Ti-based biomedical materials that possess long-lasting and effective antibacterial properties substantially, with the aim of reducing or eliminating infection [13].

The processing of titanium can be a challenging task due to its high melting point, expensive raw materials, low thermal conduction, and complex production procedures. However, the utilization of AM methods can potentially alleviate these issues, making the process more efficient and cost-effective [4]. Generally, the research in AM Titanium alloys is driven by a growing trend in alloy modification, aimed at enhancing the performance of parts produced through AM [14–19]. As a prominent member of the Titanium alloy family, there is a wealth of literature available on the processing techniques, microstructural characteristics, and mechanical properties exhibited by the Ti-6Al-4V alloy produced through Electron Beam Melting [20,21]. Currently, research on the

EBM of Ti alloys has been limited to a small number of alloys, including CP-Ti, Ti-6Al-4V, Ti-48Al-2Cr-2Nb, and Ti-6Al-2Sn-4Zr-2Mo-0.08Si [22–24]. In other works, Ti alloys have been modified in terms of microstructure by adding alloying elements during the EB-PBF process [25–28]. Aside from that, studies have demonstrated that adding appropriate amounts of certain elements during the AM of metallic biomaterials improves both mechanical and biological performance of the final product. More importantly, this approach can result in biomaterials with permanent anti-infection and anti-fouling properties [29–31].

Copper is a vital trace element in the human body that can stimulate the growth of endothelial cells, inhibit excessive arterial smooth muscle proliferation, promote bone formation, and reduce thrombosis [9,13,32]. On the other hand, Ti-Cu alloys exhibit antibacterial properties that are directly proportional to the Cu content and the surface area of the Ti_2Cu phases [9]. Research studies have shown that an antibacterial rate greater than 99% can be achieved with a Cu content of 5 wt.% or higher [33,34]. As a viable candidate for producing medical implants, LPBF method has been used to produce copper-bearing titanium alloys by various researchers [14,35–39]. Giu et al. [38] produced a range of Ti6Al4V-Cu alloys through LPBF, utilizing mixed powders of Ti6Al4V and Cu. Cu-bearing alloys showed better corrosion resistance than Cu-free ones in 0.9% NaCl solution. Also, increasing Cu content improved the alloys antibacterial activity. Ju et al. [39] developed Ti6Al4V-10Cu by LPBF that reportedly exhibited enhanced mechanical and corrosion properties, but reduced cell viability compared to samples with lower amounts of Cu. Li et al. [40] demonstrated that directed energy deposition (DED) of eutectoid and hyper-eutectoid Ti-Cu alloys produced fine, equiaxed prior-beta grains, and ultrafine eutectoid lamellae in the as-fabricated coupons, leading to promising mechanical properties. The authors found that the Ti-8.5Cu alloy exhibited exceptional antibacterial properties (99.2%) against S. algae [40]. It should be considered that increasing the copper content, however, decreases the component ductility [41,42], indicating the necessity of tailoring the chemical composition so that the mechanical behavior is not compromised over the antibacterial properties. On the other hand, processing of Cu containing materials is often a challenging procedure by laser-based AM processes. When used as an alloying element in laser-based AM processes, Cu exhibits reflectivity difficulties. Moreover, due to discrepancies in the density and viscosity of liquid titanium and copper, previous research on the in-situ alloying of Ti-Cu alloys using LPBF methods revealed the occurrence of copper-enriched localized areas [14,36,43].

However, to the best of the authors' knowledge, solely one study has been published on production of Cu-bearing Ti6Al4V alloys utilizing the Electron Beam Melting (EBM) process; Mosallanejad et al. [28] recently investigated the microstructure evolution during the in-situ alloying of Ti6Al4V-7Cu by EBM process, and reported fine and fully equiaxed prior-β grains, a chemically homogenous microstructure in terms of Cu distribution, and fine Ti_2Cu phases with different morphologies. The mentioned microstructural features were linked by the authors to the EBM being a hot process creating large melt pools. Also, the EBM produced samples generally tend to offer a reduced residual stress due to lower cooling rates compared to the other powder based AM methods, and the preheating steps occurring during the process [6]. Therefore, it is hypothesized

that the EBM components with the modified composition of Ti6Al4V-Cu, designated as Ti536, can exhibit a superior combination of antibacterial and mechanical properties. Therefore, the current work comprehensively investigates the effect of Cu on corrosion resistance, antibacterial, bioactivity and cell biocompatibility of novel Ti536 specimens which was recently developed by Mosallanejad et al. [28]. The results of this study are expected to pave the path towards developing new implant materials with multi-functions for clinical applications.

2. Materials and methods

2.1. Sample fabrication

The initial Ti6Al4V-7 wt% Cu blend, consisting of spherical powders of extra-low interstitials (ELI) grade Ti6Al4V (with a size of ≤ 106 μm and an average of 75 μm, obtained from Arcam) and high purity Cu (with a size of ≤ 2 μm and an average of 6.6 μm, obtained from Sandvik Osprey Ltd.), was subjected to a 16-hour mixing process in a jar mill. This blending process was aimed to create a homogenous mixture of the two powders, resulting in the formation of a hypoeutectoid alloy known as Ti6Al4V-7Cu during printing. It is important to note that this particular composition was chosen with the expectation of obtaining a hypoeutectoid alloy [36]. Ti6Al4V–7Cu samples were built by an Arcam A2X EBM machine. The standard Arcam A2X build theme for Ti6Al4V was employed for printing the Ti6Al4V and Ti6Al4V–7Cu samples. More details regarding the fabrication process of the samples have been mentioned in our previous work [28].

2.2. Microstructure characterization

Prior to the microstructural analysis, all samples were polished with 0.1 μm diamond paste and followed by etching with Kroll solution (HF: HNO3: H2O = 2:5:50). The resultant surfaces were observed by optical microscopy (Nikon EpipHot 300) and Scanning Electron Microscopy (SEM; Philips XL 30) equipped with energy dispersive X-ray spectrometer (EDS). Phase identification was performed by X-ray diffraction (XRD; Phillips, Netherlands) with a Cu-K_α radiation source ($\lambda = 0.154$ nm, 40 kV, 40 mA), scanning from 20 to 80° (2θ).

2.3. Corrosion studies

To evaluate the corrosion behavior of the printed samples, three methods of electrochemical impedance spectroscopy (EIS), Mott-Schottky (MS) and cyclic potentiodynamic polarization (CPP) tests were conducted in Simulated Body Fluid (SBF) at 37 ± 2°C. Table 1 provides an overview of the SBF composition used in this study. The SBF solution pH was adjusted at 7.4 by adding required amounts of 1 M HCl solution. The corrosion experiments were carried out utilizing a PARSTAT 2273 and an AMETEK potentiostat/galvanostat. The reference electrode used was Ag/AgCl saturated in potassium chloride, while a platinum sheet served as the counter electrode. The Ti6Al4V-7Cu samples working electrode for the evaluations was the sample under investigation.

Table 1. Composition of the SBF with pH adjusted at 7.4 by adding 1 M HCl, adapted from ref. [44].

Reagent	Composition (g/L)
NaCl	8.035
$NaHCO_3$	0.355
KCl	0.225
$K_2HPO_4 \cdot 3H_2O$	0.231
$MgCl_2 \cdot 6H_2O$	0.311
$CaCl_2$	0.292
Na_2SO_4	0.072

Prior to corrosion experiments, the surfaces of the samples were prepared by mechanical grinding using SiC papers up to 1200 grits. To ensure the samples cleanliness, the polished samples were ultrasonically degreased and cleaned with ethanol, rinsed with deionized water, and air dried. To establish a consistent testing environment, the samples were submerged for 45 min before each evaluation, and the open circuit potential (OCP) was measured. EIS tests were executed at OCP, utilizing a frequency range of 100 kHz to 10 mHz and an AC amplitude of 10 mV. Following the EIS process, MS relationship measurements were conducted immediately at a frequency of 1 kHz. The measurements involved sweeping from an initial potential of 1.1 $V_{Ag/AgCl}$ to a final potential of -1.5 $V_{Ag/AgCl}$ in the cathodic direction, with 10 mV/s step sizes. The CPP tests were conducted at a scanning rate of 1 mV/s, with the samples undergoing a potential range from -250 to 1500 $mV_{Ag/AgCl}$ vs. OCP. Upon reaching current density values of 100 $\mu A/cm^2$, the scan direction was reversed, and this reversed scan persisted until the samples were polarized to -250 mV below their respective OCP. All the electrochemical tests were repeated at least three times in the equivalent environment to obtain reproducible data.

2.4. Cu ion release

To evaluate the release of Cu^{2+} ions, the Ti6Al4V-7Cu samples were immersed in SBF at a temperature of 37 °C with a ratio of 3 cm^2/ml. The concentration of Cu^{2+} ion release was determined at three different time points: day 1, day 7, and day 14. Inductively Coupled Plasma Mass Spectrometry (ICP-MS; Perkin Elmer, USA) with an accuracy of 0.005 mg/L was used to measure the concentrations of the released Cu^{2+} ions.

2.5. X-ray photoelectron spectroscopy

The surface chemical compositions of Ti6Al4V and Ti6Al4V-7Cu alloys were analyzed using X-ray photoelectron spectroscopy (XPS; FlexPS, Specs, Germany). The XPS measurements utilized an Al Kα source with an energy of 1486.6 eV. To ensure the stability of the passive film, the samples were exposed to OCP for a duration of 2 hours before conducting XPS measurements, so that the surface of the sample form a naturally created a passive film [45]. The material was initially scanned in full spectrum, and then high-resolution scans were performed specifically for the Ti and Cu elements. The obtained XPS raw data were further analyzed using the CasaXPS software (Version 2.3.15, USA). For the purpose of precise interpretation, the spectra were adjusted for

binding energy referencing with respect to the C 1s peak at 284.6 eV, which served as a reference point.

2.6. Antibacterial properties

2.6.1. Plate-count method

The antibacterial efficacy of the tested samples was assessed against *Escherichia coli* ATCC25922 (*E. coli*) and *Staphylococcus aureus* ATCC25923 (*S. aureus*) using the plate count method. The samples were sterilized at 120 °C for 30 minutes and placed in a 24-well plate. A 20 µl bacterial suspension with a concentration of 10^6 CFU/mL was added to the upper surface of the samples and then covered with sterile plastic films. The plate was incubated at 37 °C with a humidity of 90% for 24 hours. Subsequently, the bacteria solution on the sample surface was diluted with 3 mL of phosphate buffer saline (PBS), and 50 µL of the diluted solution was spread onto an agar plate. The Petri dishes were incubated at 37 ± 2 °C under a humidity of 95% for an additional 24 hours to facilitate the accurate counting of bacterial colonies. The number of bacterial colonies on the plate was counted to assess the antibacterial performance of the samples. The antibacterial rate (AR) was calculated based on the following equation:

$$\mathrm{AR} = \frac{\mathrm{N_{Ti6Al4V} - N_{Ti6Al4V-7Cu}}}{\mathrm{N_{Ti6Al4V}}} * 100 \quad (1)$$

where $N_{Ti6Al4V}$ and $N_{Ti6Al4V\text{-}7Cu}$ are the average numbers of bacterial colonies on the Ti6Al4V and Ti6Al4V-7Cu samples, respectively.

2.6.2. Morphology of Bacteria

Each sample was inoculated with 100 µL of bacterial suspension. The samples were incubated at 37 °C for 24 hours, following which the bacteria and metabolites were rinsed with normal saline solution. Subsequently, the samples were treated with a 2.5% glutaraldehyde solution for a minimum of 2 hours to achieve fixation. After the fixation process, the glutaraldehyde solution was removed, and the samples were dehydrated using a series of ethanol concentrations including 30%, 50%, 70%, 90%, and 100%. The dehydrated samples were then dried in an oven. Finally, the surface morphology and distribution of bacteria on the samples were observed under a SEM after gold sputtering.

2.7. Bioactivity studies

To examine the samples bioactivity, i.e., the formation of hydroxyapatite (HA) on the surface of the printed samples, as well as the impact of Cu on the bioactivity behavior, the samples were immersed in 20 mL of SBF. The samples underwent incubation at 37 ± 2°C for 7 and 14 days under static conditions within an incubator (Memmert GmbH, Germany) to avoid exposure to light. This was done to investigate the effects of Cu and the formation of HA over time. After the immersion, the samples were extracted from the SBF, washed with distilled water, and dried

utilizing an oven. To examine the surface morphology and composition, SEM and EDX were employed.

2.8. Cell compatibility

2.8.1. Cell culture

MG63 cells (Pasteur Institute of Iran, Iran), which resemble osteoblasts, were cultured using Dulbecco's Modified Eagle Medium (DMEM), supplemented with 10% fetal bovine serum (FBS) and 1% penicillin/streptomycin (Sigma-Aldrich Co; USA). The cells were maintained in a humidified 5% CO_2 incubator in the absence of light at 37 ℃ [46]. The cell culture media was replaced 2-3 times per week, and sub-culturing was performed at 80% confluency. The rectangular 5×5 mm^2 were subjected to sterilization using 70% ethanol for 1 hour, followed by UV irradiation of both sides for 1 hour, to prepare the samples for cell seeding. Once sterilized, the samples were submerged in the cell culture medium overnight. Subsequently, the media were removed, and the cells were seeded on top of the samples.

For the experiment, cells at passages 5-7 were utilized and seeded onto the samples at a density of 5×10^3 cells/samples. To optimize the seeding efficacy, the cells were introduced in a minimal volume of media, specifically 10 µL. Subsequently, after a 10-minute interval, 500 µL of culture media was added to ensure sufficient cellular attachment to the samples. The samples were then placed in a humidified 5% CO_2 condition at 37 ± 1°C, and the media was changed every second day until the experiment concluded on day 7.

2.8.2. Cell adhesion and morphological characterization

In this study, SEM was used to examine the morphology of cells adhered to the samples surface. The cells were washed with PBS, and then fixed using 4% (w/v) paraformaldehyde (PFA) in PBS for 30 minutes at 37 ℃ to preserve their morphology and prevent any changes during the sample preparation process. The fixed samples were then dehydrated by gradually immersing them in ethanol solutions of increasing concentrations (30%, 50%, 70%, 90%, and 100%) for 30 minutes at each stage. This process removed any water that may interfere with the imaging process. The samples were then submerged in 100% hexamethyldisilane (Sigma-Aldrich Co; USA) for 30 minutes at room temperature to further dehydrate them before air drying. After dehydration, the samples were imaged using SEM to reveal the morphology of the adhered cells on the samples surface. The obtained images would allow for an assessment about the degree of cell attachment, spreading, and overall morphology on the samples surface.

2.8.3. Cell viability

To determine the relative viability of cells seeded on the samples, the MTT assay was used. The MTT assay employs a compound called methylthiazolyldiphenyl-tetrazolium bromide (MTT), which is reduced by viable cells to purple formazan crystals. The intensity of the resulting color is proportional to the number of viable cells. In this study, the viability of cells was compared to a

negative control, and MTT was obtained from Sigma-Aldrich Co; USA. To perform the MTT assay, a fresh MTT solution was prepared by dissolving 0.5 mg/ml MTT in DMEM and penicillin/streptomycin without FBS. The MTT solution was then filtered using a 0.2 µm cellulose membrane syringe filter at each time point (i.e., day 1, 3, and 7). Following the designated time points, the culture medium (DMEM) in the wells was substituted with 300 µL of MTT solution. The cells were then placed in an incubator with MTT at a temperature of 37°C under a 5% CO_2 atmosphere for four hours. This allowed sufficient time for the formation of formazan crystals. Afterward, the MTT solution was carefully removed, and the cells were solubilized with 300 µL DMSO to dissolve the formazan crystals. The absorbance of the resulting solution was measured using a 96-well plate and microplate reader at a wavelength of 630 nm to determine the relative cell viability.

In this study, the viability assay was performed with three replications for each sample and negative control. The viability was presented as a percentage of the negative control, where 100% or higher indicated no cytotoxicity (all cells were equally or more viable than in the negative control), and 0% reflected maximal cytotoxicity (all cells were dead). The optical density (OD) corresponding to cell adsorption was measured for wells containing the samples. The measurements were then compared to the control wells without the samples to determine the cell viability percentage. The formula used to calculate the cell viability is as follows:

$$\text{Cell viability} = \frac{\text{OD (sample)} - \text{OD (blank)}}{\text{OD (control)} - \text{OD (blank)}} * 100 \quad (2)$$

where OD of sample is the absorbance of the samples containing the cells; OD of blank refers to the absorbance of the blank wells with no cells or samples, and OD of control is the absorbance of the control wells with cells but no samples. By comparing the absorbance of the sample to that of the control wells, the relative viability of cells on the samples were determined.

3. Results and discussion

3.1. Microstructure

Figure 2 shows the XRD pattern of Ti6Al4V and Ti6Al4V-7Cu samples. The diffraction peaks of α-Ti and β-Ti were detected in the Ti6Al4V sample. For the Ti6Al4V–7Cu alloy, Ti_2Cu intermetallic diffraction peaks were also detected. The EDS patterns (Table 2) further confirms the existence of copper rich phases in the microstructure. As shown in Figure 2a and c, a typical acicular martensite phases can be observed in the cross section of the Ti6Al4V sample. Due to the rapid melting characteristics of EBM process, the obtained martensite structure was fine and accompanied by second phase precipitation. Significant differences were observed in the microstructure morphology for the Ti6Al4V–7Cu sample, consisting of fine grained fully equiaxed microstructure (Figure 2b) with layer-wise narrow bands of Ti_2Cu (Figure 2d), as explained in Ref. [28], where the formation of equiaxed prior-β grains was linked to the combinatory influence of a constitutionally undercooled zone formed by the rejected Cu solutes in front of the solidification

front, and a relatively lower thermal gradient in the melt pool during EB-PBF, compared with other AM techniques. Table 2 details the chemical compositions of different points, marked in Figure 2d, obtained by EDS. It was observed that the V and Cu contents at point A were comparatively lower than those at point B, while the Al content was higher than that at point B. Considering the fact that Al is an α-stabilizer, and V and Cu serve as β-stabilizers, it was deduced that point A belonged to the phase α, whereas point B was categorized as the phase β. According to the EDS results, point C contained up to 24.18 wt.% Cu and could be identified as Ti_2Cu. It can be further noticed in Figure 2 that Cu is homogenously distributed in the matrix phase, i.e., alpha, and no Cu enriched area can be traced. This observation is attributed to the large melt pool formed during the EBM process facilitating the melting of Cu powders followed by the improved mixing of the resultant melt with the molten Ti. It should be noted that, this homogeneous microstructure is obtained not only due to the facilitated mixing in the melt pool, but also due to the enhanced diffusion of Cu in a certain solidified layer upon the scanning of subsequent layers. A homogeneous distribution of Cu, as a solid solution in phase alpha, is expected to offer a huge advantage for biomedical applications [47]. Mosallanejad et al. [28] reported the formation of fine Ti_2Cu phases with different morphologies and sizes in the EBMed Ti6Al4V-7Cu samples, citing the complex thermal history experienced for a given nod during the EBM process. Generally, the formation of Ti_2Cu precipitates can occur via the eutectoid decomposition of the β phase, or precipitation from the supersaturated α phase, which is attributed to the decreasing solubility of Cu in the α phase at lower temperatures [48].

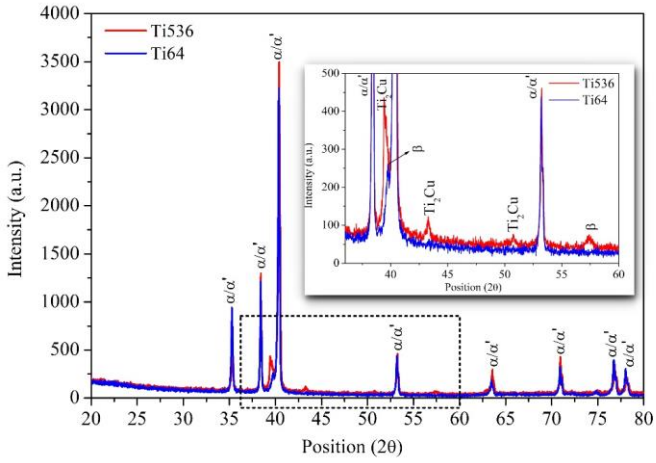

Figure 1. XRD patterns of as-built Ti6Al4V and Ti5Al3V6Cu produced in this work.

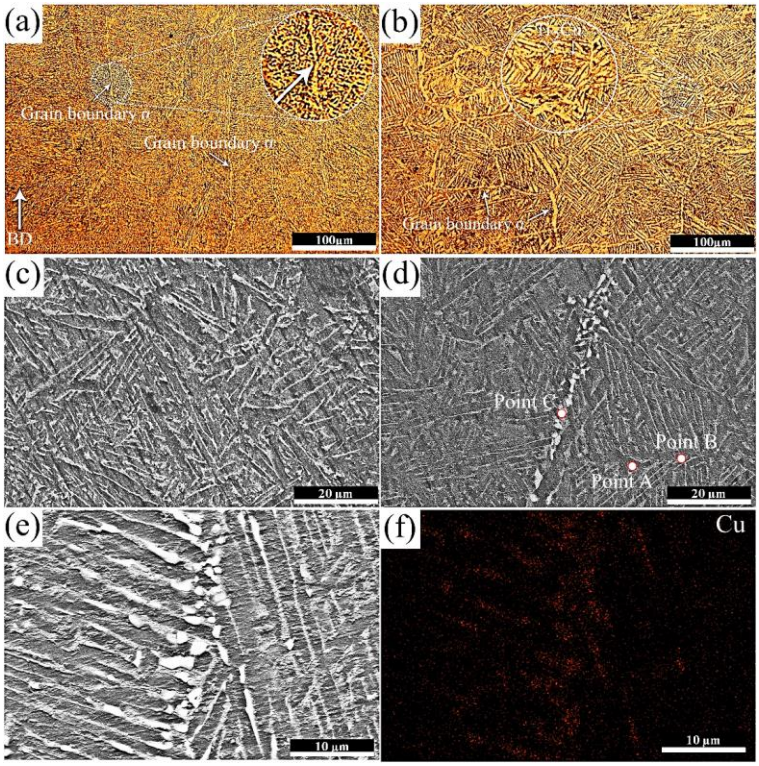

Figure 2. OM and SEM of (a,c) Ti6Al4V and (b,d) Ti6Al4V–7Cu samples, (e) higher magnification of Ti_2Cu intermetallic phases, and (f) EDS map of Cu in (e).

Table 2. Chemical composition of the spots identified in Figure 2f (wt%)

Points	Cu	V	Al	Ti	Phase
Point A	2.08	3.94	6.85	balance	α
Point B	5.45	6.26	4.48	balance	β
Point C	24.18	5.92	3.91	balance	Ti_2Cu

3.2. Corrosion

3.2.1. Open circuit potential and cyclic potentiodynamic polarization

Figure 3a shows the OCP results for Ti6Al4V and Ti6Al4V-7Cu samples in an SBF solution at 37 °C. The curves indicate that the samples spontaneously developed passive films on the surface over time (2800s) while in contact with the electrolyte. During the OCP test, the metal cations (Ti^{4+} and Cu^{2+} ions) accumulate on the electrode surface and react with the solution anions (Cl^{-}), which results in charge transfer at the metal-solution interface and thus passive film formation. Such a passivation phenomenon increases the potential in the OCP curve and reduces the kinetic

energy of the anode reaction. Previous studies have reported a similar passivation behavior, manifested by a gradual improvement of the passive film on the surface with time, upon immersion in a physiologically relevant solution for biomedical alloys [49–51].

The Ti6Al4V and Ti6Al4V-7Cu alloys showed similar CPP curves in SBF, with an active-to-passive transition at 37 °C, as shown in Figure 3b. The negative hysteresis in both Ti6Al4V and Ti6Al4V-7Cu alloys suggests that they are not prone to either pitting or crevice corrosion. Both alloys exhibited a passive stabilization region and similar pitting potentials. After analyzing the cathodic and anodic branches of the polarization curves, the corrosion potentials (E_{corr}) and corrosion current densities (I_{corr}), as well as the Tafel slopes of the anodic (βa) and cathodic (βc) branches were determined using Tafel extrapolation. I_{corr} and E_{corr} indicate the corrosion rate of the material. The polarization resistance (R_p) was calculated using the Stern-Geary Equation [52]:

$$Rp = (\beta a \times \beta c)/(2.3 \times I_{corr} \times (\beta a + \beta c)) \quad (3)$$

In addition, electrochemical parameters such as reverse potential (E_{rev}), reverse current density (I_{rev}) and repassivation potential (E_{rep}) were shown and presented in Table 3. Results indicated that in-situ alloying the Ti6Al4V by adding 7% Cu had not statistically significant impact on corrosion parameter values.

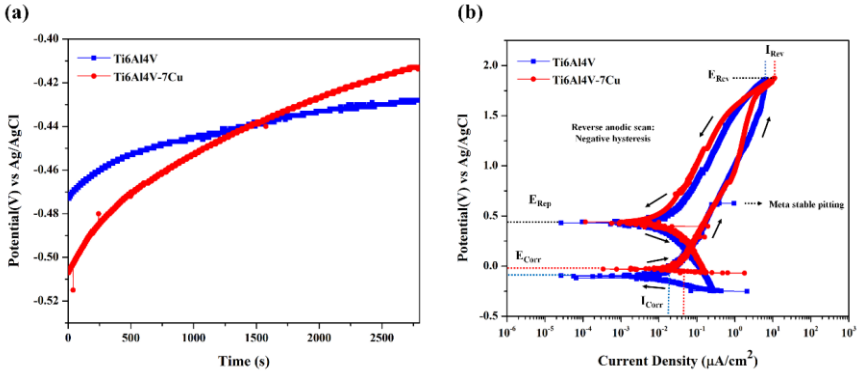

Figure 3. (a) Representative OCP measurements, and (b) cyclic potentiodynamic polarization curves (including forward and reverse scans) for Ti6Al4V and Ti6Al4V-7Cu in SBF solutions at 37 ˚C.

The corrosion behavior of materials is influenced by various factors such as microstructure, chemical composition, and processing methods. In the case of the sample under consideration, the addition of Cu resulted in two distinct mechanisms affecting its corrosion properties. The first mechanism was grain refinement, which leads to the formation of stable passive films at the grain boundaries [35,53–55], thereby enhancing the corrosion resistance. This behavior was attributed to the increased activity of electrons at the grain boundaries, which facilitated the rapid generation of passive films. On the other hand, the addition of Cu also promoted the formation of the intermetallic Ti_2Cu phase in the matrix, which created galvanic microcells between the matrix and

Ti_2Cu. In this case, the matrix acted as a cathode, and the Ti_2Cu acted as an anode. The flow of electrons from the cathode to the anode led to charge redistribution, surface potential difference (ΔE), and enhanced cathodic reactions, which increased the anodic reaction rate. Therefore, the corrosion mechanism in this case can be explained by a corrosion microcell (or corrosion galvanic couple) formed on the electrode surface between the Ti_2Cu, α-Ti, and β-Ti phases. Overall, these two competing mechanisms had a significant influence on the corrosion behavior of the sample, and their interplay needs to be considered to optimize the corrosion resistance of the material [37].

Table 3. Summary of electrochemical parameters based on cyclic potentiodynamic polarization of the samples after 1h immersion in SBF (pH 7.4) solutions at room temperature.

Materials	Parameters							
	βa (mV)	**βc (mV)**	**I_{corr} (μA/cm^2)**	**I_{rev} (μA/cm^2)**	**E_{rep} (mV)**	**E_{corr} (mV)**	**R_p (kΩ.cm^2)**	**E_{rev} (mV)**
Ti6Al4V	246±16	75±22	0.019±0.001	6.64±1.4	0.43±0.09	-0.03±0.01	1320	1.87±0.36
Ti6Al4V-7Cu	290±25	35±10	0.056±0.002	11.27±2.3	0.48±0.10	-0.09±0.03	242	1.85±0.42

Furthermore, it is worth mentioning that the physical characteristics, including the size, morphology, and distribution, of Ti_2Cu precipitates play a crucial role in determining the quality of the passive film formation that covers the Ti_2Cu phase. As a result, these characteristics have a significant impact on the corrosion properties of the sample. When the Ti_2Cu phase is uniformly distributed in the metal matrix phase, the Ti_2Cu phase can be covered by TiO_2 oxide film after the matrix dissolves and forms the passivation film. However, certain reports have stated that the formation of intermetallic compounds like Ti_2Cu phases can offer an "envelope effect", which can effectively prevent the contact between the titanium alloy and corrosive substances, thus protecting the surface of the Ti alloy and offering corrosion protection to slow down galvanic corrosion and improve corrosion resistance [56,57]. In whole, the properties of the passive film could be altered by the formation of the Ti_2Cu phase, further highlighting the importance of studying its properties.

3.2.2. Electrochemical impedance spectroscopy and Mott- Schottky analysis

Figure 4a-c presents the Nyquist and Bode modulus/phase plots of EIS tests. Nyquist plots and Bode diagrams were used to analyze the impedance spectra of Ti6Al4V and Ti6Al4V-7Cu alloys when immersed in an SBF solution at their OCP state at 37°C. The Nyquist plots showed that both alloys had a semi-circular arc dependence on their real (Z_{real}) and imaginary (Z_{imag}) components, which indicated a typical mono-layer film as observed in EIS analysis. The impedance moduli (Z) were assessed based on the size of the semi-circular arc, and the larger value of impedance indicated a higher corrosion resistance. As shown in Figure 4a, adding Cu resulted in a smaller diameter of the semi-circular arc in the Nyquist loop. This suggests that a less compact passive layer formed on the metal surface which weakened its corrosion resistance. In summary, the presence of a porous passive layer on the Ti6Al4V-7Cu metal surface resulted in reduced corrosion resistance [38].

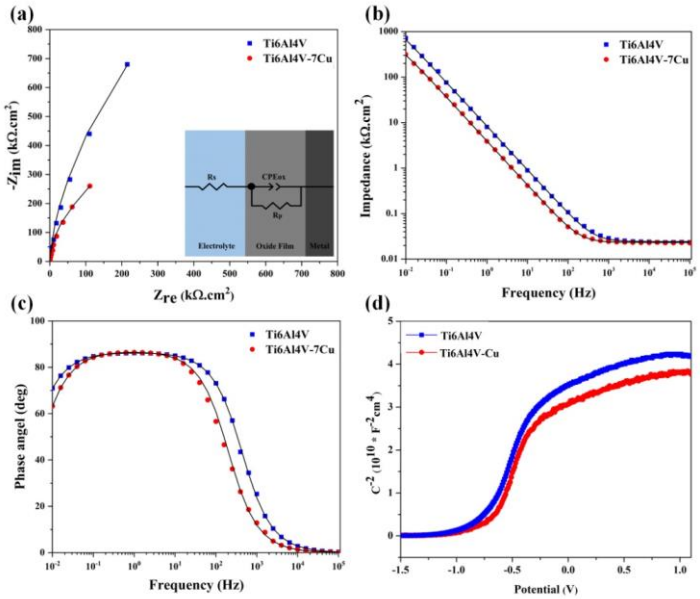

Figure 4. (a) Nyquist, (b) Bode impedance, (c) Bode phase angle, and (d) Mott-Schottky plots for Ti6Al4V and Ti6Al4V-7Cu in SBF solutions at 37 ˚C. The inset in (a) shows the equivalent electrical circuit for the analysis of the impedance spectra (Table 3).

The Bode plots obtained from Ti6Al4V and Ti6Al4V-7Cu alloys exhibited a high degree of similarity in terms of their frequency vs. impedance magnitude |Z| (Bod-Z) and frequency vs. phase angle curves (Bod-Phase). Figure 4b revealed a broad linear region with a slope of approximately -1 in the mid-frequency range (10-1000Hz), which is a typical characteristic of a mono-layer passive layer. Moreover, the Bod-Z curve of Ti6Al4V alloy had almost a steeper slope than that of Ti6Al4V-7Cu, indicating a higher barrier layer capacitance. Figure 4c revealed that both alloys had similar phase angles of 86.5˚ at medium and low frequency ranges. The Bode plots in the medium and low frequency ranges indicate the charge transport properties across the double layer at the interface between the sample and solution, as well as the passive oxide film. This result suggests that the Ti6Al4V alloy had a highly stable barrier layer of passive film. To analyze the passive layer properties, curve fitting was carried out for EIS results using a simplified Randles equivalent electrical circuit (EEC), which is a method applied in other studies as well [49,58,59]. Table 4 lists the electrochemical parameters obtained from the impedance data analysis software. The Rp value of Ti6Al4V-7Cu was significantly lower than that of the Ti6Al4V. The results revealed that adding Cu decreased Rp, which suggests that the corrosion resistance of the Ti6Al4V alloy weakened due to the formation of micro galvanic sites and porous passive layer. The fitting fairly matched the data points, as evidenced by the chi square of fitting ($\chi 2$) values being less than 10^{-3}. In the equivalent electrical circuit (shown as inset in Figure 4a, Rs represents the solution

resistance, Rp is the resistance of the oxide film, CPE denotes the constant phase element. A CPE was employed in the circuit model to account for the non-ideal capacitance of the surfaces. The impedance of the CPE is defined as [60]:

$$Z_{CPE} = Y_0(j\omega^n)^{-1} \quad (4)$$

where Y_0 is a frequency-independent constant, j is the imaginary unit ($j^2 = -1$), ω is the angular frequency, and n ($0 \leq n \leq 1$) is the phase constant exponent that represents surface irregularities. If n is equal to 0, the CPE is resistive, whereas if it is equal to 1, the CPE is capacitive. The effective capacity (C_{eff}) for each passive layer was calculated using the Brug model [61]:

$$C_{eff} = \sqrt[n]{Q.R_T^{1-n}} \quad (5)$$

where R_T is the total resistance sum (R_s and R_p). The capacitance can be related to the thickness of the film (L_{SS}) using the following equation:

$$Lss = \frac{\varepsilon\varepsilon_0 A}{C_{eff}} \quad (6)$$

where ε represents the relative permittivity of the material (around 45 for TiO_2 passive film [50,62]) ε_0 denotes the permittivity of the vacuum (8.854×10^{-14} Fcm^{-1}) and A represents the surface area. According to Equation 5, an increase in C_{eff} indicates a decrease in the thickness of the passive layer. This reduction in thickness can be attributed to the presence of Cu, which may have affected the formation and stability of the passive layer. The copper element can create micro galvanic sites, which can accelerate the corrosion rate and cause the passive layer to become unstable, leading to a decrease in its thickness [56]. The decrease in the thickness of the passive layer can result in a lower corrosion resistance of the Ti6Al4V-7Cu alloy, as observed in the experimental results. In conclusion, it can be said that the random distribution of the Ti_2Cu phase had a negative effect on passive layer properties.

Table 4. EIS fitting parameters (average and standard deviation of three independent samples)

Materials	Parameters						
	Rs (Ωcm^2)	**CPE (Y_0, $\mu Fcm^{-2}s^{-n}$)**	**C_{eff} (μFcm^{-2})**	**N**	**R_p ($M\Omega cm^2$)**	**L_{SS} (nm)**	**X^2 (10^{-3})**
Ti6Al4V	24.28±0.68	20.36±4.31	14.82±2.51	0.95±0.06	2.48±0.22	1.82±0.20	0.55±0.08
Ti6Al4V-7Cu	23.24±0.95	42.82±6.78	23.47±3.18	0.92±0.09	0.75±0.13	1.07±0.24	0.86±0.08

Mott-Schottky analysis was used to probe the electrical characteristics of the passive film by measuring the capacitance variation that occurs in an electrochemical interface as its DC voltage is changed [63]. From Mott-Schottky plots, a linear relationship is expected between $1/C^2$ and the

applied potential (*E*) for the passive film, which can be described by the following two equations for different types of semiconductors:

$$\frac{1}{C_{SC}^{2}} = \frac{2}{e\varepsilon\varepsilon_0 N_D}\left(E - E_{fb} - \frac{k_B T}{e}\right) \quad (7)$$

$$\frac{1}{C_{SC}^{2}} = -\frac{2}{e\varepsilon\varepsilon_0 N_A}\left(E - E_{fb} - \frac{k_B T}{e}\right) \quad (8)$$

Where N_D and N_A represent the charge carrier densities of the donor and acceptor, respectively, and C_{sc} represents the space charge capacitance, e is the elementary charge (1.6×10^{-19} C), k is the Boltzmann constant, T is the absolute temperature and E_{fb} is the flat band potential.

Figure 4d shows the M-S curves for passive film on Ti6Al4V and Ti6Al4V–7Cu alloys in SBF at 37 °C at -1.5 $V_{Ag/AgCl}$ to 1.1 $V_{Ag/AgCl}$. There was a linear region with a positive slope in M-S plots. Based on the point defect model (PDM) [64], the passive films show n-type semiconducting behavior for both samples indicating that the dominant defects in the oxide layer are donors, which determine the rate of active dissolution of the electrode surface. Regarding the donor species, oxygen vacancies could be dominant in the oxide film due to its lower formation energy compared with Ti^{n+} interstitials [49,65]. It is reported that the donor concentrations (N_D) are inversely proportional to the slope obtained from the linear part of the M-S plot. So, N_D can be estimated using equation (9):

$$N_D = \frac{2}{\varepsilon.\varepsilon_0.e.a} \quad (9)$$

where a is the slope in n-type region. The N_D of the passive films was estimated to be $4.43 \pm (1.27) \times 10^{20}$ cm^{-3} and $8.95 \pm (1.42) \times 10^{20}$ cm^{-3} for Ti6Al4V and Ti6Al4V-7Cu, respectively. It is worth mentioning that the value for N_D in previous literature is from 10^{18} to 10^{23} cm^{-3}, depending on the oxide film potential formation and the electrolyte used [65,66]. It was clearly observed that N_D increased by adding Cu to EBM Ti6Al4V alloys. According to the PDM model [67], once the passive film formed on the electrode surface, the subsequent growth process is determined by the flux of oxygen vacancies in the film. Charge transfer plays a crucial role in influencing the density of oxygen vacancies. The increase in oxygen vacancy density corresponds to an increased defect density, which, in turn, reduces the stability of the passive film [65]. Compared to Ti6Al4V, adding Cu and formation of Ti_2Cu contribute to an increased presence of elemental copper within the passive film. This higher percentage of elemental copper enhances the probability of charge transfer from elemental copper to Cu^{2+}, leading to a higher defect density within the passive film [68].Consequently, the passive film exhibits an increased reactivity with halide anions, especially chloride ions (Cl^{-}) [35,56,69]. In line with this observation, Han et al. found that precipitates can serve as preferential sites for the initiation of passive film breakdown [70]. Therefore, it is reasonable to infer that the formation of Ti_2Cu results in localized defects, which in turn promote the release of metallic elements and hinder the formation of a protective passive film [37]. Thus, it can be deduced from EIS and M-S analysis that the passive film on Ti6Al4V-7Cu will be thinner with a higher defect density and lower corrosion resistance than Ti6Al4V. These results further

show that the effect of Cu content on the corrosion resistance of Ti6Al4V alloy, as determined from the CPP plots, was consistent with the results obtained from the EIS and M-S tests.

3.3 Metal ion release and surface analysis

Figure 5a shows the Cu^{2+} dissolution concentration and the dissolution rate of EBM Ti6Al4V-7Cu sample in SBF solution for 14 days. The concentration increased gradually while the dissolution rate decreased sharply with the immersion time. The release of Cu ions was much lower than the minimum acceptable intake of Cu for an adult recommended by World Health Organization (approximately 1.3 mg/day) [71,72].

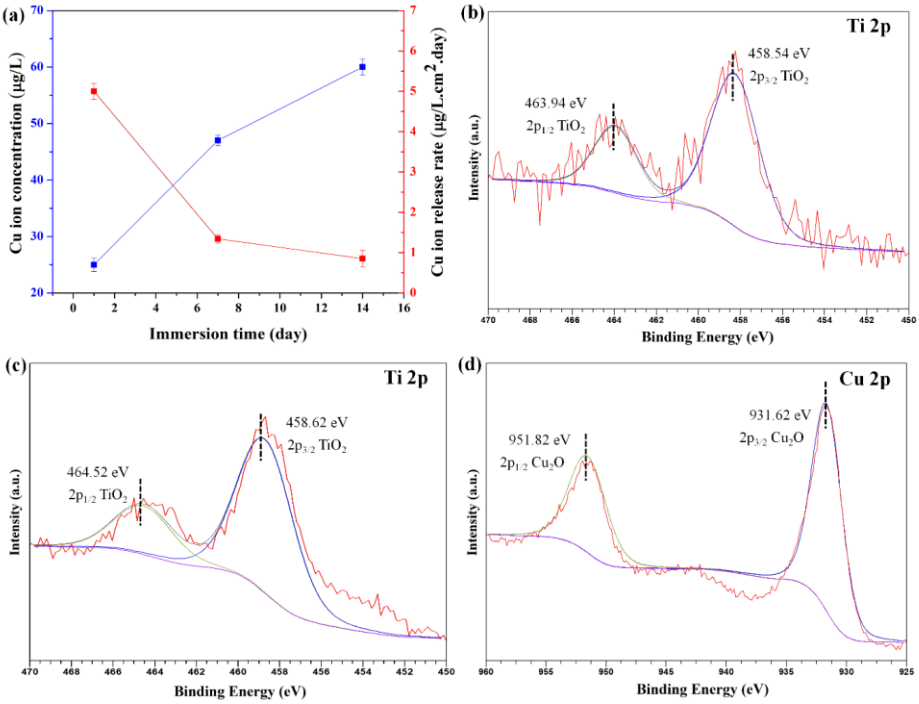

Figure 5. (a) Cu ion release concentration and Cu ion release rate from Ti6Al4V-7Cu alloy, (b) XPS spectra of Ti2p for Ti6Al4V, (c) XPS spectra of Ti2p for Ti6Al4V-7Cu alloy, and (d) XPS spectra of Cu2p for Ti6Al4V-7Cu alloy.

As mentioned in the previous section, the excellent corrosion resistance of the Ti-based alloys may be attributed to the spontaneous formation of a passive film on their surfaces. Chemical composition of the passive film outermost surface formed on Ti6Al4V and Ti6Al4V-7Cu alloys were examined by XPS. Figure 5b-d shows the high-resolution XPS spectrum corresponding to

Ti2p and Cu 2p. In the Ti spectra for Ti6Al4V shown in Figure 5b, $Ti2p_{1/2}$ at 463.94 eV and $Ti2p_{3/2}$ at 458.54 eV, both corresponding to TiO_2, were detected, indicating that TiO_2 was formed on the surface. Similarly, the Ti2p XPS spectra (Figure 5c) of Ti6Al4V-Cu sample were composed of TiO_2. The peaks that appeared at a binding energy of 458.62 eV for $Ti2p_{3/2}$ and 464.52 eV for $Ti2p_{1/2}$ were assigned to TiO_2 state. In Figure 4d, the high-resolution spectra of Cu show that Cu_2O was formed on the surface with the $Cu2p_{3/2}$ peak at 931.62 eV and the $Cu2p_{1/2}$ peak at 951.82 eV. It is well accepted that the Cu-rich phase, i.e., Ti_2Cu in titanium alloys, is the major source of Cu oxides on the surface [37,40,73]. Therefore, it can be inferred from the XPS results that a thin oxide layer mainly consisting of TiO_2 and Cu_2O was formed on the Ti6Al4V-7Cu alloy surface.

3.4 Antibacterial Properties

Figure 6 shows images of typical S. aureus and E. coli bacteria colonies and the antibacterial rates after 24-h incubation at 37 ± 0.5 °C on both samples. Numerous colonies were observed on the agar plates containing Ti6Al4V, indicating the lack of any antibacterial effect. In contrast, the Ti6Al4V-7Cu sample exhibited only a few colonies, suggesting the complete elimination of both S. aureus and E. coli bacteria after 24 hours of incubation. This outcome confirms that the addition of copper to the alloy enhanced the antibacterial properties of the EBMed product. The antibacterial rates calculated from the data in Figure 6 clearly illustrate that the Ti6Al4V-7Cu samples displayed a significant reduction in bacterial growth, exceeding 99%. This remarkable decrease in bacterial rate demonstrates strong antibacterial behavior.

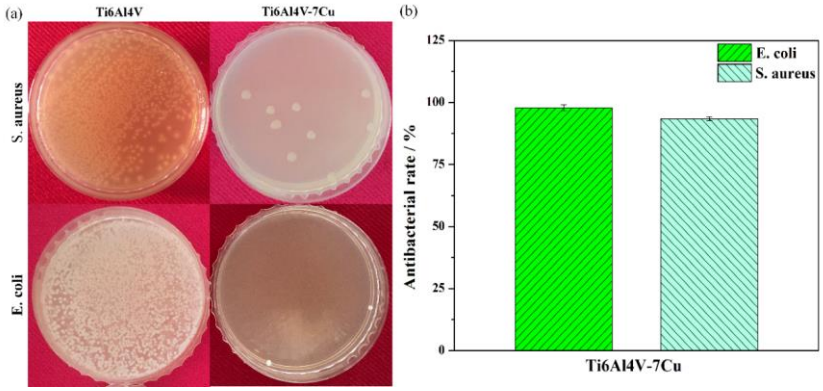

Figure 6. (a) Typical bacteria colony cultured for 24 h on Ti6Al4V and TI6Al4V-7Cu samples, and (b) the calculated antibacterial rate.

Figure 7 shows the morphologies of S. aureus and E. coli on the sample surfaces after a 24hr incubation period, as observed by SEM. On the surfaces of Ti6Al4V sample, a large number of bacteria were observed, with S. aureus appearing as spherical and E. coli as rod-shaped clusters. This indicates that most of both bacteria grew well and were in good condition on the surface. In contrast, on the surfaces of Ti6Al4V-7Cu samples, there was a significant decrease in the number

of bacteria, and the bacterial morphology became irregular. Some bacteria showed signs of shrinkage and deformation, displaying a collapsed appearance with disrupted cell walls and cytoplasm leakage. These observations confirm the strong antibacterial properties of the Ti6Al4V-7Cu sample against both bacteria types. It has also been shown in previous reports that the antibacterial activity of Ti-Cu alloy is significantly dependent on the Cu content [35,39,74], and that the volume fraction, particle size and shape of Ti_2Cu phase in Ti-Cu alloy plays a critical role in the alloys antibacterial properties [75,76].

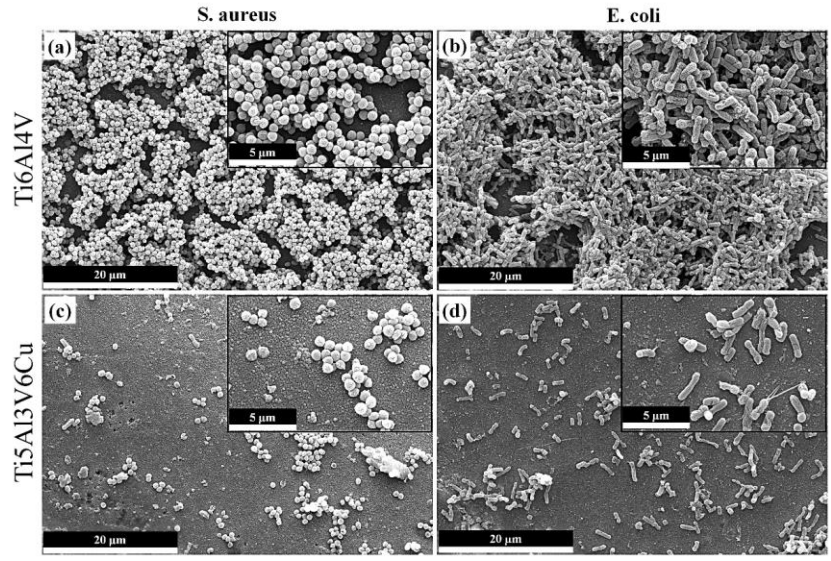

Figure 7. Morphology of *S. aureus and E. coli* cultured on the samples surface for 24 h.

In summary, the possible antibacterial mechanism of the Ti6Al4V-7Cu sample can mainly attributed to the combined effect of the Cu ion release, surface potential difference caused by micro-galvanic corrosion cells and the contact-killing effect of Cu oxides on the surface [40,56,77]. Figure 8 shows a schematic diagram of the antibacterial mechanisms.

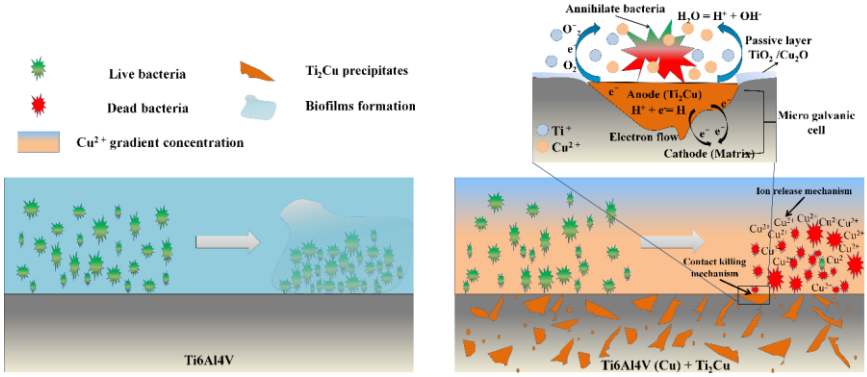

Figure 8. Schematic diagram of Cu ion release caused by micro-galvanic corrosion and contact killing mechanism of Ti6Al4V-7Cu alloy during the antibacterial process.

To further explain the potential antibacterial mechanisms (Figure 8), the feasible reactions between the existing species should be taken into account. The electrochemical results indicate that the corrosion behavior of Ti-Cu alloy is predominantly governed by the corrosion of Ti_2Cu, which results in the release of Cu and Ti ions. The corrosion process of Ti_2Cu can be primarily attributed to two factors, namely, the consumption of cathodic oxygen and the degradation of the anodic metal [78,79].The corrosion reaction responsible for consuming cathodic oxygen can be represented as follows [68]:

$$O_2 + 2H_2O + 4e^- = 4OH^- \quad (1)$$

Then, the free OH^- reacts with Ti_2Cu through anodic degradation. In the first step, Ti_2Cu degrades into Ti^{4+} and Cu^{2+} ions [80,81].

$$Ti_2Cu + 10OH^- = 2Ti^{4+} + Cu^{2+} + 4H_2O + 10e^- \quad (2)$$

Subsequently, considering that Ti^{4+} has a stronger affinity for O^{2-} than Cu^{2+} does, Ti^{4+} reacts with OH^- generating TiO_2, followed by formation of Cu_2O on the surface [65,82].

$$Ti^{4+} + 4\ OH^- = TiO_2 + 2H_2O \quad (3)$$

$$Cu^{2+} + 2\ OH^- = Cu_2O + 2H_2O \quad (4)$$

The antibacterial mechanism, based on the release of copper ions, can occur in the following way according to the first step of the anodic reaction (reaction 2): Cu^{2+} ions can extract electrons from bacteria. These electrons bind to the plasma membrane due to electrostatic attraction, and then penetrate the cell membrane through the opening or closing of the membrane channels. [56,83].However, it is well recognized that the concentration of Cu ions must be greater than $1 \times 10{-}5$ $molL^{-1}$ (or 640 μgL^{-1}) to obtain a substantial antibacterial rate [9,13,84] As shown in Figure 5a, the Cu ions released from Ti6Al4V-7Cu alloy are far less than the critical Cu concentration required for desirable antibacterial performance. In other words, such a small amount of released

Cu ions cannot account for the high antibacterial rate. This finding implies that other factors also contributed to the antibacterial properties. It was mentioned earlier that the micro-galvanic corrosion cells between Ti_2Cu particulate and matrix caused directional movement of charges due to surface potential difference (Figure 8). According to the reported findings, it is commonly observed that electrons tend to flow from the cathodic phase (matrix) to the anodic phase (Ti_2Cu particulate) [40,56,83]. This redistribution of charge results in a difference in surface potential [9]. Hence, a significant accumulation of bacteria and microorganisms on a material's surface may lead to the formation of biofilms. Such biofilms can alter the pH levels of the surrounding area. Furthermore, these biofilms may cause the hydrolysis of water, leading to a dynamic change in the distribution of dissolved oxygen ions in the system. [56,85], as depicted in Figure 8. Furthermore, the micro-galvanic cell on the surface of the Ti6Al4V-7Cu alloy will produce electrons (reaction 2). Thus, as reported in previous reports, the electrons donated by the Cu-rich phase (Ti_2Cu particulate) are consumed and depleted by H^+ (Figure 8). Afterward, the growth of the bacteria chain is disturbed by the Proton Motive Force (PMF) activity of bacteria, ultimately leading to the antibacterial effect [56,74,83,86].

Moreover, it can be said that the direct interaction of the Ti6Al4V-7Cu alloy with the bacterial cell membrane resulted in an enhanced antibacterial activity. From the second anodic reaction, the release of Cu^{2+} ions from the surface caused the formation of copper oxide (CuO, Cu_2O) on the surface. It is reported that the redox cycling between different copper species, Cu, Cu^+, and Cu^{2+}, could result in an imbalance of the inner and outer membrane potential [87], thus promoting the formation of reactive oxygen species (ROS) within the bacteria and leading to a contact-killing effect [56,83,85]. ROS is a common intracellular signaling molecule as a product of the imbalance of oxygen in the cell by oxidation. Hydrogen peroxide (H_2O_2), superoxide anion (O_2^-), and hydroxyl radical (OH') are the three common types of ROS [56]. Indeed, as reported, Cu was an important cofactor for many oxidases that act as a catalyst in producing ROS following the reactions below:

$$Cu^+ + H_2O_2 = Cu^{2+} + OH^- + OH' \quad (5)$$

$$H_2O_2 + O_2^- = O_2 + OH^- + OH' \quad (6)$$

Consequently, the superoxide radicals (O2−) and H_2O_2 formed in response to oxidative stress, induce the formation of hydroxyl radicals (OH') [85,88], which disrupt the integrity of cell membranes, inducing cell wall damage and protein damage and ultimately leading to the death of bacteria [83,89,90]. Furthermore, Mathews et al. [91] reported that the reduction potentials of Cu/Cu^+, Cu^+/Cu^{2+} fall within the biological reduction potentials range, which result in the production of ROS species.

Overall, based on Figure 8 and the above discussion, it could be assumed that the bacteria could not adhere to the surface due to the presence of the Ti_2Cu phase and the release of Cu^{2+} ions, and hence the Ti6Al4V-7Cu implant is expected to have a long-lasting antibacterial role in the human body.

3.5. In-vitro bioactivity test

To evaluate the bioactivity, both samples were immersed in SBF for 7 and 14 days, as a part of in vitro tests [44]. As mentioned in previous reports, the growth of HA on the sample surfaces is a measure of the bioactivity level [92,93]. Figure 8 shows SEM images of the top views of Ti6Al4V and Ti6Al4V-7Cu samples after immersion in SBF. Both samples exhibited flake-like deposits on their surfaces. The images in Figure 9 illustrate a comparable gradual accumulation of precipitates on both samples, with the entire surface appearing to be coated with a relatively thick layer of HA after 14 days. The EDX analysis shown in Figure 10 presents the Ca/P ratio in the deposited layers. The atomic Ca/P ratio increased progressively for all samples with exposure time, and no significant differences were observed among the samples. After 14 days, the Ca/P ratio of Ti6Al4V and Ti6Al4V-7Cu reached 1.52 ± 0.12 and 1.61 ± 0.04, respectively, which are close to the natural HA ratio of 1.67 [44].

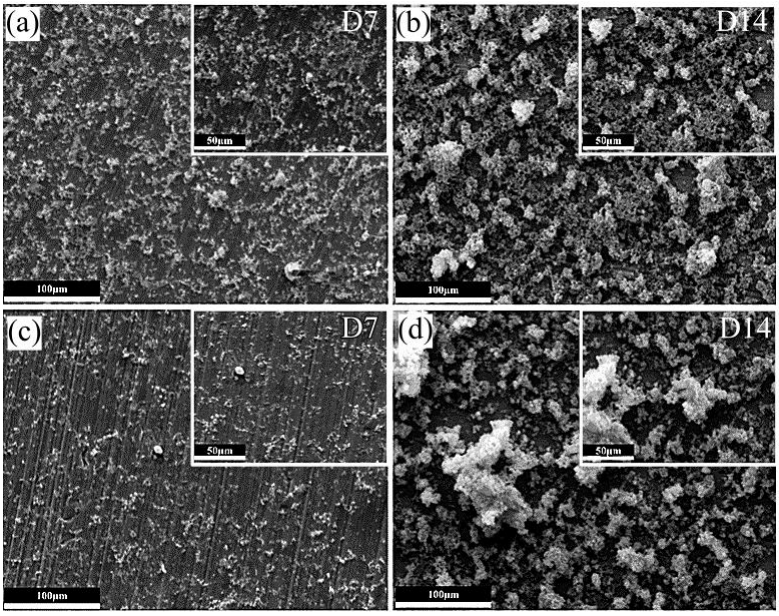

Figure 9. SEM images of (a-b) Ti6Al4V and (c-d) Ti6Al4V-7Cu samples after immersion in simulated body fluid for 7 (D7), and 14 (D14) days at 37 °C. Insets in the images provide an overview at a higher magnification.

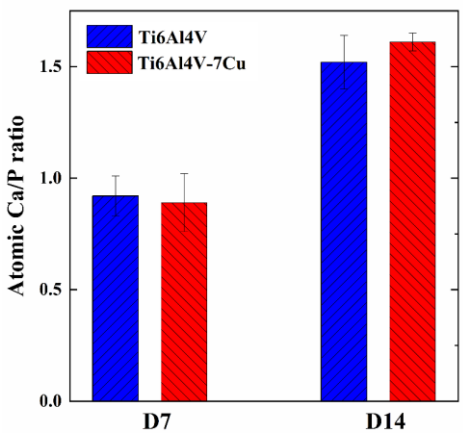

Figure 10. EDS results showing the atomic Ca/P ratio for Ti6Al4V and Ti6Al4V-7Cu samples, after immersion in SBF for 7 (D7), and 14 (D14) days at 37°C. The error bars indicate the standard deviation of triplicate measurements.

3.6. Biocompatibility test

Studies have indicated that the existence of a certain concentration of copper ions can induce cytotoxicity, leading to cell death. Thus, it is crucial to investigate the compatibility of copper-containing titanium alloys with cells when biomedical applications are intended [13,94–96]. Figure 11 shows the results of the MTT assay, which was used to assess cell viability after 1, 3, and 7 days. As shown in Figure 11a, optical density (OD) values increased for both samples with the incubation time, indicating that cells were in healthy condition during the whole experimental period. There were no significant differences in the OD values observed between the Ti6Al4V-7Cu and Ti6Al4V samples at all investigated time points. Figure 11b shows the calculated cell viability of MG63 cells on both samples. After 1 day of cultivation, both samples displayed fully viable cells, i.e., around 100%. However, the viability of cells significantly decreased in both samples after 3 and 7 days of cultivation. On day 7, the cell viability values ranged from 80% to 92%, which is relatively low compared to the values obtained on day 1 and day 3. However, no significant differences were noticed in cell viability values for the Ti6Al4V sample and the Ti6Al4V-7Cu samples at all cultivation time points. According to the Standard Gb/T 16886.5 [97], which provides guidelines for the evaluation of the cytotoxicity of biomedical materials, the materials exhibit cell viability between 90% and 100% are classified as Grade 0, and materials that exhibit cell viability between 75% and 90% are classified as Grade 1. A biomedical material is considered to have no significant toxicity for cells when it is classified as Grade 0 or Grade 1 based on the cytotoxicity scale. In previous studies [32,78,94], it has been suggested that a cell viability of 75% or higher can be reported as a sign of no cytotoxicity. According to the findings of this study (Figure 11b), the materials used in the experiment were classified as Grade 0 on day 1, indicating that Cu did not have any significant cytotoxic effects on cells at that point in time.

During days 3 and 7 of the study, all samples almost were rated as Grade 1 on the cytotoxicity scale. In addition, cells on the surface reached 100% confluency on day 7. This means that cells had no more room to grow and increase in number compared to the control, meanwhile, some of the cells did not survive. Therefore, this may explain the observed decrease in viability on day7 in comparison to day 1.

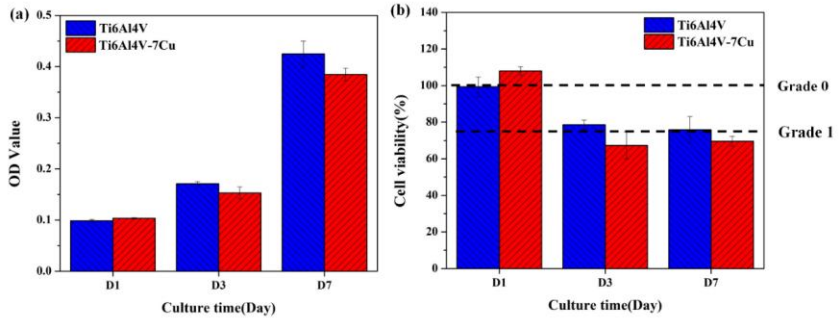

Figure 11. Variation of (a) OD values, and (b) cell viability values of Ti6Al4V and Ti6Al4V-7Cu alloys with incubation time.

Furthermore, the morphology of cells can provide insight into their behavior and interactions with the surrounding environment. The contact and interaction between cells and biomaterial surfaces play a crucial role in physiological processes. In this study, Figure 12 depicts the morphology of MG63 cells that were cultured on the Ti6Al4V and Ti6Al4V-7Cu samples for 1 and 7 days, respectively. After one day of incubation, a semi-confluent layer of cells was observed on the surfaces of both samples. On the 7th day, a sharp increase in the rate of cell adhesion and proliferation was observed for both samples. The cell morphology of the Ti6Al4V and Ti6Al4V-7Cu samples did not exhibit any discernible differences, indicating that the presence of Cu in the Ti6Al4V-7Cu samples did not affect the cell morphology during 1 day and 7 days of cultivation. In addition to cell attachment and proliferation, the study observed cell-to-cell interactions, characterized by the presence of filopodia and lamellipodia extending from the cells. Previous studies have emphasized the importance of filopodia, which are frequently observed in migratory cells [98]. Filopodia play crucial roles in various cellular processes, including cytoskeletal organization, cell division, and transport mechanisms. These dynamic cellular extensions aid in the expansion of the cell surface and facilitate the exchange of substances [99,100]. Consequently, the existence of these cytoskeletal components serves as an indication of normal cellular activity and implies that the cells were able to retain their regular functions and behavior when in contact with the surfaces of both the Ti6Al4V and Ti6Al4V-7Cu samples. In addition, Zhang et al. have indicated that the released Cu ion from Cu-bearing titanium alloys would not affect the MG63 cell if the concentration of the released Cu ion is well controlled in the range between 30-227 μg/L [94]. This behavior is consistent with the results obtained in the Cu ion concentration section of this study (Figure 5a).

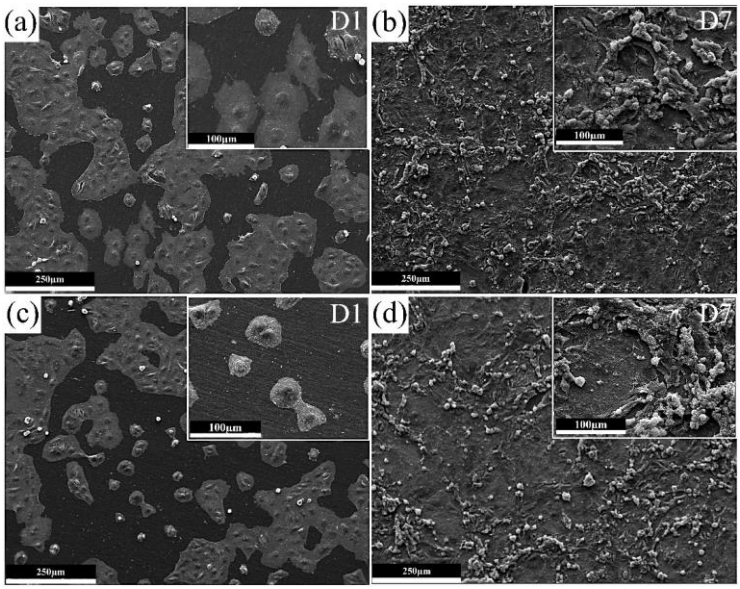

Figure 12. Morphology of MG63 cells formed on (a-b) Ti6Al4V and (c-d) Ti6Al4V-7Cu alloys after 1 and 7 days of incubation.

In summary, based on the aforementioned findings and analysis, it can be inferred that the biocompatibility of Ti6Al4V-7Cu alloy has been found to be comparable to that of Ti6Al4V, indicating its potential suitability for use in implant materials. However, it is imperative to conduct extensive long-term in vitro assessments and in vivo studies to comprehensively evaluate the biocompatibility of this alloy. Such investigations will provide detailed insights into its biocompatibility profile.

4. Conclusions

In conclusion, this study provides a comprehensive evaluation of a Cu-modified Ti6Al4V alloy, focusing on its microstructure, corrosion properties, antibacterial behavior, and biological responses. The findings contribute to a better understanding of the material's potential for biomedical applications. Enhanced antibacterial properties without compromising cell biocompatibility and corrosion behavior is reported. The following concluding remarks can be highlighted:

- The study successfully demonstrated the feasibility of producing a novel Ti-based implant with enhanced biomedical properties using EB-PBF method.
- The corrosion test results indicated that the Ti_2Cu precipitates in the Ti536 microstructure caused a slight increase in corrosion rate, a decrease in corrosion resistance, and the

Commented [MM1]: I tried to deepen the conclusion but I think you can do it better than me, given the field being corrosion and bioactivity experiments. For doing so, you may also find the following hints insightful:

- Can you also add some quantitative results?
- Can you add more concluding remarks? You have a lot of findings, don't be shy 😊 present them.
- If am an implant producer and want to choose between Ti64 and Ti64-7Cu, do your conclusions help me or they make more confused?

formation of a thinner passive film compared with Cu-free Ti6Al4V alloy. Moreover, the overall corrosion behavior of Ti536 samples was suggested to be also influenced by prior-β grain refinement leading to the formation of passive films at grain boundaries and thus alleviating the corrosion behavior of the sample.

- Based on the Mott-Schottky test, it was found that while both samples exhibit typical n-type semiconductive properties, the calculated density of oxygen vacancy for the Ti6Al4V sample was lower than that of the Ti536 sample, indicating a more defective passive film on the latter. The XPS results indicated that though the passive film formed on the Ti6Al4V mainly consisted of TiO_2, the Cu addition introduced Cu_2O in the passive film of Ti536 alloy.
- Ti536 exhibited strong and stable antibacterial properties against E. coli and S. aureus. The possible antibacterial mechanism of the Ti536 sample was mainly attributed to the combined effect of Cu ion release, the surface potential difference caused by micro-galvanic corrosion cells, and the formation of Cu_2O in the passive film.

References

[1] T. DebRoy, H.L. Wei, J.S. Zuback, T. Mukherjee, J.W. Elmer, J.O. Milewski, A.M. Beese, A. Wilson-Heid, A. De, W. Zhang, Additive manufacturing of metallic components – Process, structure and properties, Prog. Mater. Sci. 92 (2018) 112–224. https://doi.org/10.1016/j.pmatsci.2017.10.001.

[2] H. Attar, S. Ehtemam-Haghighi, D. Kent, M.S. Dargusch, Recent developments and opportunities in additive manufacturing of titanium-based matrix composites: A review, Int. J. Mach. Tools Manuf. 133 (2018) 85–102. https://doi.org/10.1016/j.ijmachtools.2018.06.003.

[3] M. Salmi, Additive Manufacturing Processes in Medical Applications, Materials (Basel). 14 (2021) 191. https://doi.org/10.3390/ma14010191.

[4] E. Davoodi, H. Montazerian, A.S. Mirhakimi, M. Zhianmanesh, O. Ibhadode, S.I. Shahabad, R. Esmaeilizadeh, E. Sarikhani, S. Toorandaz, S.A. Sarabi, R. Nasiri, Y. Zhu, J. Kadkhodapour, B. Li, A. Khademhosseini, E. Toyserkani, Additively manufactured metallic biomaterials, Bioact. Mater. 15 (2022) 214–249. https://doi.org/10.1016/j.bioactmat.2021.12.027.

[5] S. Mellor, L. Hao, D. Zhang, Additive manufacturing: A framework for implementation, Int. J. Prod. Econ. 149 (2014) 194–201. https://doi.org/10.1016/j.ijpe.2013.07.008.

[6] L.E. Murr, S.M. Gaytan, D.A. Ramirez, E. Martinez, J. Hernandez, K.N. Amato, P.W. Shindo, F.R. Medina, R.B. Wicker, Metal Fabrication by Additive Manufacturing Using Laser and Electron Beam Melting Technologies, J. Mater. Sci. Technol. 28 (2012) 1–14. https://doi.org/https://doi.org/10.1016/S1005-0302(12)60016-4.

[7] D.E. Reichman, J.A. Greenberg, Reducing surgical site infections: a review., Rev. Obstet. Gynecol. 2 (2009) 212–21. https://doi.org/10.3909/riog0084.

[8] J. GRISCHKE, J. EBERHARD, M. STIESCH, Antimicrobial dental implant functionalization strategies —A systematic review, Dent. Mater. J. 35 (2016) 545–558.

https://doi.org/10.4012/dmj.2015-314.

[9] E. Zhang, X. Zhao, J. Hu, R. Wang, S. Fu, G. Qin, Antibacterial metals and alloys for potential biomedical implants, Bioact. Mater. 6 (2021) 2569–2612. https://doi.org/10.1016/j.bioactmat.2021.01.030.

[10] J. Jiao, S. Zhang, X. Qu, B. Yue, Recent Advances in Research on Antibacterial Metals and Alloys as Implant Materials, Front. Cell. Infect. Microbiol. 11 (2021). https://doi.org/10.3389/fcimb.2021.693939.

[11] L. Zhao, P.K. Chu, Y. Zhang, Z. Wu, Antibacterial coatings on titanium implants, J. Biomed. Mater. Res. Part B Appl. Biomater. 91B (2009) 470–480. https://doi.org/10.1002/jbm.b.31463.

[12] P.A. Norowski, J.D. Bumgardner, Biomaterial and antibiotic strategies for peri-implantitis: A review, J. Biomed. Mater. Res. Part B Appl. Biomater. 88B (2009) 530–543. https://doi.org/10.1002/jbm.b.31152.

[13] E.-L. Zhang, S. Fu, R.-X. Wang, H.-X. Li, Y. Liu, Z.-Q. Ma, G.-K. Liu, C.-S. Zhu, G.-W. Qin, D.-F. Chen, Role of Cu element in biomedical metal alloy design, Rare Met. 38 (2019) 476–494. https://doi.org/10.1007/s12598-019-01245-y.

[14] M.H. Mosallanejad, B. Niroumand, A. Aversa, D. Manfredi, A. Saboori, Laser Powder Bed Fusion in-situ alloying of Ti-5%Cu alloy: Process-structure relationships, J. Alloys Compd. 857 (2021) 157558. https://doi.org/10.1016/j.jallcom.2020.157558.

[15] M.H. Mosallanejad, B. Niroumand, A. Aversa, A. Saboori, In-Situ Alloying in Laser-Based Additive Manufacturing Processes: A Critical Review, J. Alloys Compd. 872 (2021) 159567. https://doi.org/10.1016/j.jallcom.2021.159567.

[16] P. Barriobero-Vila, J. Gussone, A. Stark, N. Schell, J. Haubrich, G. Requena, Peritectic titanium alloys for 3D printing, Nat. Commun. 9 (2018) 1–9. https://doi.org/10.1038/s41467-018-05819-9.

[17] R. Banerjee, P.C. Collins, D. Bhattacharyya, S. Banerjee, H.L. Fraser, Microstructural evolution in laser deposited compositionally graded a / b titanium-vanadium alloys, Acta Mater. 51 (2003) 3277–3292. https://doi.org/10.1016/S1359-6454(03)00158-7.

[18] T. Zhang, Z. Huang, T. Yang, H. Kong, J. Luan, A. Wang, D. Wang, W. Kuo, Y. Wang, C.T. Liu, In situ design of advanced titanium alloy with concentration modulations by additive manufacturing, Science (80-.). 374 (2021) 478–482. https://doi.org/10.1126/science.abj3770.

[19] D. Zhao, C. Han, Y. Li, J. Li, K. Zhou, Q. Wei, J. Liu, Y. Shi, Improvement on mechanical properties and corrosion resistance of titanium-tantalum alloys in-situ fabricated via selective laser melting, J. Alloys Compd. 804 (2019) 288–298. https://doi.org/10.1016/j.jallcom.2019.06.307.

[20] L. Zhang, Y. Liu, S. Li, Y. Hao, Additive Manufacturing of Titanium Alloys by Electron Beam Melting: A Review, Adv. Eng. Mater. 20 (2018) 1700842. https://doi.org/10.1002/adem.201700842.

[21] S. Liu, Y.C. Shin, Additive manufacturing of Ti6Al4V alloy: A review, Mater. Des. 164 (2019) 107552. https://doi.org/10.1016/j.matdes.2018.107552.

[22] S. Biamino, A. Penna, U. Ackelid, S. Sabbadini, O. Tassa, P. Fino, M. Pavese, P. Gennaro, C. Badini, Electron beam melting of Ti–48Al–2Cr–2Nb alloy: Microstructure and mechanical properties investigation, Intermetallics. 19 (2011) 776–781. https://doi.org/10.1016/j.intermet.2010.11.017.

[23] A. Saboori, D. Gallo, S. Biamino, P. Fino, M. Lombardi, An overview of additive manufacturing of titanium components by directed energy deposition: Microstructure and mechanical properties, Appl. Sci. 7 (2017). https://doi.org/10.3390/app7090883.

[24] M. Galati, S. Defanti, A. Saboori, G. Rizza, E. Tognoli, N. Vincenzi, A. Gatto, L. Iuliano, An investigation on the processing conditions of Ti-6Al-2Sn-4Zr-2Mo by electron beam powder bed fusion: Microstructure, defect distribution, mechanical properties and dimensional accuracy, Addit. Manuf. 50 (2022) 102564. https://doi.org/https://doi.org/10.1016/j.addma.2021.102564.

[25] Z. Mahbooba, H. West, O. Harrysson, A. Wojcieszynski, R. Dehoff, P. Nandwana, T. Horn, Effect of Hypoeutectic Boron Additions on the Grain Size and Mechanical Properties of Ti-6Al-4V Manufactured with Powder Bed Electron Beam Additive Manufacturing, JOM. 69 (2017) 472–478. https://doi.org/10.1007/s11837-016-2210-9.

[26] T. Fujieda, Y. Cui, K. Aoyagi, Y. Koizumi, A. Chiba, Electron beam melting of boron-modified Ti–6Al–2Sn–4Zr–2Mo–0.1Si alloy with superior tensile strength and oxidation resistance at elevated temperatures, Materialia. 4 (2018) 367–372. https://doi.org/10.1016/j.mtla.2018.10.013.

[27] X. Li, Z. Yao, X. Tao, M. Yao, S. Zhang, Developing Cu modified Ti6Al4V alloys with a combination of high strength and ductility by electron beam freeform fabrication, Vacuum. 194 (2021) 110638. https://doi.org/10.1016/j.vacuum.2021.110638.

[28] M.H. Mosallanejad, B. Niroumand, C. Ghibaudo, S. Biamino, A. Salmi, P. Fino, A. Saboori, In-situ alloying of a fine grained fully equiaxed Ti-based alloy via Electron Beam Powder Bed Fusion Additive Manufacturing process, Addit. Manuf. 56 (2022) 102878. https://doi.org/10.1016/j.addma.2022.102878.

[29] A. Bandyopadhyay, K.D. Traxel, M. Lang, M. Juhasz, N. Eliaz, S. Bose, Alloy design via additive manufacturing: Advantages, challenges, applications and perspectives, Mater. Today. 52 (2022) 207–224. https://doi.org/10.1016/j.mattod.2021.11.026.

[30] T.M. Pollock, A.J. Clarke, S.S. Babu, Design and Tailoring of Alloys for Additive Manufacturing, Metall. Mater. Trans. A. 51 (2020) 6000–6019. https://doi.org/10.1007/s11661-020-06009-3.

[31] A. Behjat, M. Shamanian, F. Sadeghi, L. Iuliano, A. Saboori, Additive manufacturing of a novel in-situ alloyed AISI316L-Cu stainless steel: Microstructure and antibacterial properties, Mater. Lett. 355 (2024) 135363. https://doi.org/10.1016/j.matlet.2023.135363.

[32] S. Moniri Javadhesari, S. Alipour, M.R. Akbarpour, Biocompatibility, osseointegration, antibacterial and mechanical properties of nanocrystalline Ti-Cu alloy as a new orthopedic material, Colloids Surfaces B Biointerfaces. 189 (2020) 110889. https://doi.org/10.1016/j.colsurfb.2020.110889.

[33] E. Zhang, X. Wang, M. Chen, B. Hou, Effect of the existing form of Cu element on the mechanical properties, bio-corrosion and antibacterial properties of Ti-Cu alloys for

biomedical application, Mater. Sci. Eng. C. 69 (2016) 1210–1221. https://doi.org/10.1016/j.msec.2016.08.033.

[34] A. Macpherson, X. Li, P. McCormick, L. Ren, K. Yang, T.B. Sercombe, Antibacterial Titanium Produced Using Selective Laser Melting, Jom. 69 (2017) 2719–2724. https://doi.org/10.1007/s11837-017-2589-y.

[35] H. Ji, M.C. Zhao, B. Xie, Y.C. Zhao, D. Yin, C. Gao, C. Shuai, A. Atrens, Corrosion and antibacterial performance of novel selective-laser-melted (SLMed) Ti-xCu biomedical alloys, J. Alloys Compd. 864 (2021) 158415. https://doi.org/10.1016/j.jallcom.2020.158415.

[36] A.M. Vilardell, I. Yadroitsev, I. Yadroitsava, M. Albu, N. Takata, M. Kobashi, P. Krakhmalev, D. Kouprianoff, G. Kothleitner, A. du Plessis, Manufacturing and characterization of in-situ alloyed Ti6Al4V(ELI)-3 at.% Cu by laser powder bed fusion, Addit. Manuf. 36 (2020). https://doi.org/10.1016/j.addma.2020.101436.

[37] X. Xu, Y. Lu, S. Li, S. Guo, M. He, K. Luo, J. Lin, Copper-modified Ti6Al4V alloy fabricated by selective laser melting with pro-angiogenic and anti-inflammatory properties for potential guided bone regeneration applications, Mater. Sci. Eng. C. 90 (2018) 198–210. https://doi.org/10.1016/j.msec.2018.04.046.

[38] L. Liu, M. He, X. Xu, C. Zhao, Y. Gan, J. Lin, J. Luo, J. Lin, Preliminary study on the corrosion resistance, antibacterial activity and cytotoxicity of selective-laser-melted Ti6Al4V-xCu alloys, Mater. Sci. Eng. C. 72 (2017) 631–640. https://doi.org/10.1016/j.msec.2016.11.126.

[39] J. Ju, R. Zan, Z. Shen, C. Wang, P. Peng, J. Wang, B. Sun, B. Xiao, Q. Li, S. Liu, T. Yang, Remarkable bioactivity, bio-tribological, antibacterial, and anti-corrosion properties in a Ti-6Al-4V-xCu alloy by laser powder bed fusion for superior biomedical implant applications, Chem. Eng. J. 471 (2023) 144656. https://doi.org/10.1016/j.cej.2023.144656.

[40] J. Li, D. Zhang, X. Chen, D. Xu, D. Qiu, F. Wang, M. Easton, Laser directed energy deposited, ultrafine-grained functional titanium-copper alloys tailored for marine environments: Antibacterial and anti-microbial corrosion studies, J. Mater. Sci. Technol. 166 (2023) 21–33. https://doi.org/10.1016/j.jmst.2023.05.020.

[41] D. Zhang, D. Qiu, M.A. Gibson, Y. Zheng, H.L. Fraser, D.H. StJohn, M.A. Easton, Additive manufacturing of ultrafine-grained high-strength titanium alloys, Nature. 576 (2019) 91–95. https://doi.org/10.1038/s41586-019-1783-1.

[42] T. Aoki, I.C.I. Okafor, I. Watanabe, M. Hattori, Y. Oda, T. Okabe, Mechanical properties of cast Ti-6Al-4V-XCu alloys, J. Oral Rehabil. 31 (2004) 1109–1114. https://doi.org/10.1111/j.1365-2842.2004.01347.x.

[43] I. Yadroitsev, P. Krakhmalev, I. Yadroitsava, Titanium Alloys Manufactured by In Situ Alloying During Laser Powder Bed Fusion, JOM. 69 (2017) 2725–2730. https://doi.org/10.1007/s11837-017-2600-7.

[44] T. Kokubo, H. Takadama, How useful is SBF in predicting in vivo bone bioactivity?, Biomaterials. 27 (2006) 2907–2915. https://doi.org/10.1016/j.biomaterials.2006.01.017.

[45] Z.B. Wang, H.X. Hu, C.B. Liu, Y.G. Zheng, The effect of fluoride ions on the corrosion behavior of pure titanium in 0.05M sulfuric acid, Electrochim. Acta. 135 (2014) 526–535.

https://doi.org/10.1016/j.electacta.2014.05.055.

[46] A. Kocijan, I. Milošev, B. Pihlar, The influence of complexing agent and proteins on the corrosion of stainless steels and their metal components, J. Mater. Sci. Mater. Med. 14 (2003) 69–77. https://doi.org/10.1023/A:1021505621388.

[47] L. Fowler, O. Janson, H. Engqvist, S. Norgren, C. Öhman-Mägi, Antibacterial investigation of titanium-copper alloys using luminescent Staphylococcus epidermidis in a direct contact test, Mater. Sci. Eng. C. 97 (2019) 707–714. https://doi.org/10.1016/j.msec.2018.12.050.

[48] X. Yao, Q.Y. Sun, L. Xiao, J. Sun, Effect of Ti2Cu precipitates on mechanical behavior of Ti–2.5Cu alloy subjected to different heat treatments, J. Alloys Compd. 484 (2009) 196–202. https://doi.org/10.1016/j.jallcom.2009.04.095.

[49] Y. Zhang, J. Li, H. Xu, L. Feng, T. Zhang, Dynamic evolution of oxide film on selective laser melted Ti–6Al–4V alloy, J. Alloys Compd. 849 (2020) 156622. https://doi.org/10.1016/j.jallcom.2020.156622.

[50] A. Bordbar-Khiabani, M. Gasik, Electrochemical behavior of additively manufactured patterned titanium alloys under simulated normal, inflammatory, and severe inflammatory conditions, J. Mater. Res. Technol. 26 (2023) 356–370. https://doi.org/10.1016/j.jmrt.2023.07.113.

[51] P. Qin, Y. Liu, T.B. Sercombe, Y. Li, C. Zhang, C. Cao, H. Sun, L.C. Zhang, Improved Corrosion Resistance on Selective Laser Melting Produced Ti-5Cu Alloy after Heat Treatment, ACS Biomater. Sci. Eng. 4 (2018) 2633–2642. https://doi.org/10.1021/acsbiomaterials.8b00319.

[52] M. Stern, A.L. Geaby, Electrochemical Polarization, J. Electrochem. Soc. 104 (1957) 56. https://doi.org/10.1149/1.2428496.

[53] A. Behjat, M. Shamanian, A. Taherizadeh, E. Lannunziata, S. Bagherifard, E. Gadalińska, A. Saboori, L. Iuliano, Microstructure-electrochemical behavior relationship in post processed AISI316L stainless steel parts fabricated by laser powder bed fusion, J. Mater. Res. Technol. 23 (2023) 3294–3311. https://doi.org/10.1016/j.jmrt.2023.01.229.

[54] G. Sander, J. Tan, P. Balan, O. Gharbi, D.R. Feenstra, L. Singer, S. Thomas, R.G. Kelly, J.R. Scully, N. Birbilis, Corrosion of Additively Manufactured Alloys: A Review, CORROSION. 74 (2018) 1318–1350. https://doi.org/10.5006/2926.

[55] A. Fattah-alhosseini, O. Imantalab, G. Ansari, The role of grain refinement and film formation potential on the electrochemical behavior of commercial pure titanium in Hank's physiological solution, Mater. Sci. Eng. C. 71 (2017) 827–834. https://doi.org/10.1016/j.msec.2016.10.072.

[56] P. Mahmoudi, M.R. Akbarpour, H.B. Lakeh, F. Jing, M.R. Hadidi, B. Akhavan, Antibacterial Ti–Cu implants: A critical review on mechanisms of action, Mater. Today Bio. 17 (2022) 100447. https://doi.org/10.1016/j.mtbio.2022.100447.

[57] W.R. Osório, C.M. Freire, R. Caram, A. Garcia, The role of Cu-based intermetallics on the pitting corrosion behavior of Sn-Cu, Ti-Cu and Al-Cu alloys, Electrochim. Acta. 77 (2012) 189–197. https://doi.org/10.1016/j.electacta.2012.05.106.

[58] M.H. Mosallanejad, S. Sanaei, M. Atapour, B. Niroumand, L. Iuliano, A. Saboori,

Microstructure and Corrosion Properties of CP-Ti Processed by Laser Powder Bed Fusion under Similar Energy Densities, Acta Metall. Sin. (English Lett. 35 (2022) 1453–1464. https://doi.org/10.1007/s40195-022-01376-9.

[59] V. Dehnavi, J.D. Henderson, C. Dharmendra, B.S. Amirkhiz, D.W. Shoesmith, J.J. Noël, M. Mohammadi, Corrosion Behaviour of Electron Beam Melted Ti6Al4V: Effects of Microstructural Variation, J. Electrochem. Soc. 167 (2020) 131505.

[60] P. Córdoba-Torres, T.J. Mesquita, O. Devos, B. Tribollet, V. Roche, R.P. Nogueira, On the intrinsic coupling between constant-phase element parameters α and Q in electrochemical impedance spectroscopy, Electrochim. Acta. 72 (2012) 172–178. https://doi.org/10.1016/j.electacta.2012.04.020.

[61] G.J. Brug, A.L.G. van den Eeden, M. Sluyters-Rehbach, J.H. Sluyters, The analysis of electrode impedances complicated by the presence of a constant phase element, J. Electroanal. Chem. Interfacial Electrochem. 176 (1984) 275–295. https://doi.org/10.1016/S0022-0728(84)80324-1.

[62] S. Ren, C. Du, Z. Liu, X. Li, J. Xiong, S. Li, Effect of fluoride ions on corrosion behaviour of commercial pure titanium in artificial seawater environment, Appl. Surf. Sci. 506 (2020) 144759. https://doi.org/10.1016/j.apsusc.2019.144759.

[63] A. Fattah-alhosseini, F. Soltani, F. Shirsalimi, B. Ezadi, N. Attarzadeh, The semiconducting properties of passive films formed on AISI 316 L and AISI 321 stainless steels: A test of the point defect model (PDM), Corros. Sci. 53 (2011) 3186–3192. https://doi.org/10.1016/j.corsci.2011.05.063.

[64] D.D. Macdonald, The history of the Point Defect Model for the passive state: A brief review of film growth aspects, Electrochim. Acta. 56 (2011) 1761–1772. https://doi.org/10.1016/j.electacta.2010.11.005.

[65] X. Gai, Y. Bai, J. Li, S. Li, W. Hou, Y. Hao, X. Zhang, R. Yang, R.D.K. Misra, Electrochemical behaviour of passive film formed on the surface of Ti-6Al-4V alloys fabricated by electron beam melting, Corros. Sci. 145 (2018) 80–89. https://doi.org/10.1016/j.corsci.2018.09.010.

[66] D.-I. Seo, J.-B. Lee, Localized corrosion and repassivation behaviors of additively manufactured titanium alloys in simulated biomedical solutions, Npj Mater. Degrad. 7 (2023) 44. https://doi.org/10.1038/s41529-023-00363-4.

[67] D.D. Macdonald, The Point Defect Model for the Passive State, J. Electrochem. Soc. 139 (1992) 3434–3449. https://doi.org/10.1149/1.2069096.

[68] C. Xin, N. Wang, Y. Chen, B. He, Q. Zhao, L. Chen, Y. Tang, B. Luo, Y. Zhao, X. Yang, Biological corrosion behaviour and antibacterial properties of Ti-Cu alloy with different Ti2Cu morphologies for dental applications, Mater. Des. 215 (2022) 110540. https://doi.org/10.1016/j.matdes.2022.110540.

[69] X. Zhang, J. Zhao, T. Xi, M.B. Shahzad, C. Yang, K. Yang, Dissolution and repair of passive film on Cu-bearing 304L stainless steels immersed in H2SO4 solution, J. Mater. Sci. Technol. 34 (2018) 2149–2159. https://doi.org/10.1016/j.jmst.2018.02.017.

[70] J. Han, Y. Cheng, W. Tu, T.-Y. Zhan, Y. Cheng, The black and white coatings on Ti-6Al-4V alloy or pure titanium by plasma electrolytic oxidation in concentrated silicate

electrolyte, Appl. Surf. Sci. 428 (2018) 684–697. https://doi.org/10.1016/j.apsusc.2017.09.109.

[71] W.H. W.H. Organization, Trace Elements in Human Nutrition and Health, Organization1996., No Title, (n.d.).

[72] P. TRUMBO, A.A. YATES, S. SCHLICKER, M. POOS, Dietary Reference Intakes, J. Am. Diet. Assoc. 101 (2001) 294–301. https://doi.org/10.1016/S0002-8223(01)00078-5.

[73] L. Li, Y. Chen, Y. Lu, S. Qin, G. Huang, T. Huang, J. Lin, Effect of heat treatment on the corrosion resistance of selective laser melted Ti6Al4V3Cu alloy, J. Mater. Res. Technol. 12 (2021) 904–915. https://doi.org/10.1016/j.jmrt.2021.03.041.

[74] I. Burghardt, F. Lüthen, C. Prinz, B. Kreikemeyer, C. Zietz, H.G. Neumann, J. Rychly, A dual function of copper in designing regenerative implants, Biomaterials. 44 (2015) 36–44. https://doi.org/10.1016/j.biomaterials.2014.12.022.

[75] E. Zhang, X. Wang, M. Chen, B. Hou, Effect of the existing form of Cu element on the mechanical properties, bio-corrosion and antibacterial properties of Ti-Cu alloys for biomedical application, Mater. Sci. Eng. C. 69 (2016) 1210–1221. https://doi.org/10.1016/j.msec.2016.08.033.

[76] J.H. Wu, K.K. Chen, C.Y. Chao, Y.H. Chang, J.K. Du, Effect of Ti2Cu precipitation on antibacterial property of Ti-5Cu alloy, Mater. Sci. Eng. C. 108 (2020) 110433. https://doi.org/10.1016/j.msec.2019.110433.

[77] J.W. Sim, J.H. Kim, C.H. Park, J.-K. Hong, J.-T. Yeom, S.W. Lee, Effect of phase conditions on tensile and antibacterial properties of Ti-Cu alloys with Ti2Cu intermetallic compound, J. Alloys Compd. 926 (2022) 166823. https://doi.org/10.1016/j.jallcom.2022.166823.

[78] R. Liu, Y. Tang, L. Zeng, Y. Zhao, Z. Ma, Z. Sun, L. Xiang, L. Ren, K. Yang, In vitro and in vivo studies of anti-bacterial copper-bearing titanium alloy for dental application, Dent. Mater. 34 (2018) 1112–1126. https://doi.org/10.1016/j.dental.2018.04.007.

[79] Y. Zhou, S. Zhang, L. Guo, S. Xu, H. Lu, F. Gao, Studies on the Effect of a Newly Synthesized Schiff Base Compound on the Corrosion of Copper in 3% NaCl Solution, Int. J. Electrochem. Sci. 10 (2015) 2072–2087. https://doi.org/10.1016/S1452-3981(23)04830-7.

[80] W.R. Osório, A. Cremasco, P.N. Andrade, A. Garcia, R. Caram, Electrochemical behavior of centrifuged cast and heat treated Ti–Cu alloys for medical applications, Electrochim. Acta. 55 (2010) 759–770. https://doi.org/10.1016/j.electacta.2009.09.016.

[81] L. Ren, Z. Ma, M. Li, Y. Zhang, W. Liu, Z. Liao, K. Yang, Antibacterial Properties of Ti–6Al–4V–xCu Alloys, J. Mater. Sci. Technol. 30 (2014) 699–705. https://doi.org/10.1016/j.jmst.2013.12.014.

[82] X. Gai, Y. Bai, S. Li, W. Hou, Y. Hao, X. Zhang, R. Yang, R.D.K. Misra, In-situ monitoring of the electrochemical behavior of cellular structured biomedical Ti-6Al-4V alloy fabricated by electron beam melting in simulated physiological fluid, Acta Biomater. 106 (2020) 387–395. https://doi.org/10.1016/j.actbio.2020.02.008.

[83] X. Zhang, C. Yang, K. Yang, Contact Killing of Cu-Bearing Stainless Steel Based on Charge Transfer Caused by the Microdomain Potential Difference, ACS Appl. Mater.

Interfaces. 12 (2020) 361–372. https://doi.org/10.1021/acsami.9b19596.

[84] C. Ning, X. Wang, L. Li, Y. Zhu, M. Li, P. Yu, L. Zhou, Z. Zhou, J. Chen, G. Tan, Y. Zhang, Y. Wang, C. Mao, Concentration Ranges of Antibacterial Cations for Showing the Highest Antibacterial Efficacy but the Least Cytotoxicity against Mammalian Cells: Implications for a New Antibacterial Mechanism, Chem. Res. Toxicol. 28 (2015) 1815–1822. https://doi.org/10.1021/acs.chemrestox.5b00258.

[85] Z. Zhang, X.-R. Zhang, T. Jin, C.-G. Yang, Y.-P. Sun, Q. Li, K. Yang, Antibacterial mechanism of Cu-bearing 430 ferritic stainless steel, Rare Met. 41 (2022) 559–569. https://doi.org/10.1007/s12598-021-01751-y.

[86] Y. Xie, M. Lu, S. Cui, H. Yu, L. Wang, H. Ke, E. Zhang, Construction of a Rough Surface with Submicron Ti2Cu Particle on Ti-Cu Alloy and Its Effect on the Antibacterial Properties and Cell Biocompatibility, Metals (Basel). 12 (2022) 1008. https://doi.org/10.3390/met12061008.

[87] G. Grass, C. Rensing, M. Solioz, Metallic Copper as an Antimicrobial Surface, Appl. Environ. Microbiol. 77 (2011) 1541–1547. https://doi.org/10.1128/AEM.02766-10.

[88] J.M. Slauch, How does the oxidative burst of macrophages kill bacteria? Still an open question, Mol. Microbiol. 80 (2011) 580–583. https://doi.org/10.1111/j.1365-2958.2011.07612.x.

[89] Z. Zhang, G. Zheng, H. Li, L. Yang, X. Wang, G. Qin, E. Zhang, Anti-bacterium influenced corrosion effect of antibacterial Ti-3Cu alloy in Staphylococcus aureus suspension for biomedical application, Mater. Sci. Eng. C. 94 (2019) 376–384. https://doi.org/10.1016/j.msec.2018.09.057.

[90] A.F. Seixas, A.P. Quendera, J.P. Sousa, A.F.Q. Silva, C.M. Arraiano, J.M. Andrade, Bacterial Response to Oxidative Stress and RNA Oxidation, Front. Genet. 12 (2022). https://doi.org/10.3389/fgene.2021.821535.

[91] S. Mathews, M. Hans, F. Mücklich, M. Solioz, Contact Killing of Bacteria on Copper Is Suppressed if Bacterial-Metal Contact Is Prevented and Is Induced on Iron by Copper Ions, Appl. Environ. Microbiol. 79 (2013) 2605–2611. https://doi.org/10.1128/AEM.03608-12.

[92] H. Pan, X. Zhao, B.W. Darvell, W.W. Lu, Apatite-formation ability – Predictor of "bioactivity"?, Acta Biomater. 6 (2010) 4181–4188. https://doi.org/10.1016/j.actbio.2010.05.013.

[93] A.A. Zadpoor, Relationship between in vitro apatite-forming ability measured using simulated body fluid and in vivo bioactivity of biomaterials, Mater. Sci. Eng. C. 35 (2014) 134–143. https://doi.org/10.1016/j.msec.2013.10.026.

[94] E. Zhang, L. Zheng, J. Liu, B. Bai, C. Liu, Influence of Cu content on the cell biocompatibility of Ti–Cu sintered alloys, Mater. Sci. Eng. C. 46 (2015) 148–157. https://doi.org/10.1016/j.msec.2014.10.021.

[95] Z. Yi, Y. Liu, Y. Ma, Z. Liu, H. Sun, X. Zhou, R. Kang, V.A.M. Cristino, Q. Wang, Surface treatment of 3D printed Cu-bearing Ti alloy scaffolds for application in tissue engineering, Mater. Des. 213 (2022) 110350. https://doi.org/10.1016/j.matdes.2021.110350.

[96] J. Yang, H. Qin, Y. Chai, P. Zhang, Y. Chen, K. Yang, M. Qin, Y. Zhang, H. Xia, L. Ren, B. Yu, Molecular mechanisms of osteogenesis and antibacterial activity of Cu-bearing Ti alloy in a bone defect model with infection in vivo, J. Orthop. Transl. 27 (2021) 77–89. https://doi.org/10.1016/j.jot.2020.10.004.

[97] B.E. of M.D.P. Chinese Standard Gb/T 16886.5-2003, 2003. 5: Test for In Vitro Cytotoxicity, No Title, (n.d.).

[98] P.K. Mattila, P. Lappalainen, Filopodia: molecular architecture and cellular functions, Nat. Rev. Mol. Cell Biol. 9 (2008) 446–454. https://doi.org/10.1038/nrm2406.

[99] G. Jacquemet, H. Hamidi, J. Ivaska, Filopodia in cell adhesion, 3D migration and cancer cell invasion, Curr. Opin. Cell Biol. 36 (2015) 23–31. https://doi.org/10.1016/j.ceb.2015.06.007.

[100] S.A. Harris, R.J. Enger, L.B. Riggs, T.C. Spelsberg, Development and characterization of a conditionally immortalized human fetal osteoblastic cell line, J. Bone Miner. Res. 10 (2009) 178–186. https://doi.org/10.1002/jbmr.5650100203.